ADVANCED ENERGY MATERIALS
www.advenergymat.de

Diffusion Limitation of Lithium Metal and Li–Mg Alloy Anodes on LLZO Type Solid Electrolytes as a Function of Temperature and Pressure

Thorben Krauskopf, Boris Mogwitz, Carolin Rosenbach, Wolfgang G. Zeier, and Jürgen Janek**

The morphological instability of the lithium metal anode is the key factor restricting the rate capability of lithium metal solid state batteries. During lithium stripping, pore formation takes place at the interface due to the slow diffusion kinetics of vacancies in the lithium metal. The resulting current focusing increases the internal cell resistance and promotes fast lithium penetration. In this work, galvanostatic electrochemical impedance spectroscopy is used to investigate operando the morphological changes at the interface by analysis of the interface capacitances. Therewith, the effect of temperature, stack pressure, and chemical modification is investigated. The work demonstrates that introducing 10 at% Mg into the lithium metal anode can effectively prevent contact loss. Nevertheless, a fundamental kinetic limitation is also observed for the Li-rich alloy, namely the diffusion controlled decrease of the lithium metal concentration at the interface. An analytical diffusion model is used to describe the temperature-dependent delithiation kinetics of Li–Mg alloys. Overall, it is shown that different electrode design concepts should be considered. Mg alloying can increase lithium utilization, when no external pressure is applied while pure lithium metal is superior for setups that allow stack pressures in the MPa range.

1. Introduction

For the development of solid state batteries (SSBs) with competitive energy density compared to conventional lithium ion batteries (LIBs) with liquid electrolyte, it is of utmost importance to enable the lithium metal anode with high rate capability.[1–4] While in LIBs with liquid electrolytes, lithium dendrite growth and low Coulombic efficiency prevent the use of lithium metal as an anode material,[3,5–11] solid electrolytes (SEs) had been predicted to be able to block dendrite growth due to their high shear modulus.[12,13] In this context, $Li_7La_3Zr_2O_{12}$ (LLZO) type garnet SEs[14] have attracted great attention as they combine high ionic conductivity with sufficient electrochemical stability against lithium metal, which prevents fast degradation and growth of a resistive interphase.[15,16] Nevertheless, certain issues at the lithium|solid electrolyte interface remain unsolved.[17,18] Lithium penetration through garnet-type SEs currently limits the possible charge rates.[19–23] In this context, it was found that good contact to a small reservoir of lithium metal is highly beneficial to prevent inhomogeneous lithium nucleation, which then reduces the lithium penetration susceptibility.[24] All previous results underline the need for sufficient and homogeneous contact between metal and SE during battery operation. Thus, it is of upmost importance for lithium metal solid-state battery development to prevent pore formation and growth at the anode interface during battery discharge.[24–26]

Indeed, while the intrinsic charge transfer kinetics of the lithium|LLZO interface was found to be sufficiently fast for practical applications (R_{int} < 2 Ωcm²),[26,27] recent work shows that the morphological instability of the (pure) lithium metal anode on solid electrolytes under anodic load is an inherent, fundamental problem that needs to be solved for battery designs that do not allow high operation pressures in the MPa range.[26,28]

The morphological instability stems from the vacancy injection into lithium metal during anodic dissolution, which is a general phenomenon of parent metal electrodes.[29,30] It leads to contact loss and unwanted local current constriction during cell discharge. Therefore, transport of lithium in the lithium metal anode itself needs to be better understood and tuned to further increase the rate capability of cells with a lithium metal anode (i.e., to per-cycle areal capacities of 5 mAh cm^{-2} at current densities ranging to 10 mA cm^{-2}).[31] However, the currently run, predominantly short-term lithium shuttling experiments on

T. Krauskopf, Dr. B. Mogwitz, C. Rosenbach, Dr. W. G. Zeier, Prof. J. Janek
Institute of Physical Chemistry
Justus-Liebig-University Giessen
Heinrich-Buff-Ring 17, D-35392 Giessen, Germany
E-mail: thorben.krauskopf@phys.chemie.uni-giessen.de; juergen.janek@phys.chemie.uni-giessen.de
Dr. W. G. Zeier, Prof. J. Janek
Center for Materials Research (ZfM)
Justus-Liebig-University Giessen
Heinrich-Buff-Ring 16, D-35392 Giessen, Germany
The ORCID identification number(s) for the author(s) of this article can be found under https://doi.org/10.1002/aenm.201902568.

DOI: 10.1002/aenm.201902568

symmetric cells are far away from the practical necessary conditions. They are often performed with only limited cumulative charges passed, at which the kinetic limitations do not necessarily become critical. We like to note that only a few publications deal with the self-diffusion limitation in the lithium anode itself.[26,32,33]

Quite a number of studies reported on lithium alloying interlayers, such as Ge, Al, Sn, Au, Si, Mg, and Ag, aiming to improve the interface kinetics.[34–40] The focus of these works was not on the diffusion properties of the lithium alloy interlayer, despite the fact they can in principle show higher lithium diffusion coefficients than pure lithium, increasing the diffusion limited current density and reducing the problem of pore formation at the interface.[41,42] A closer look shows that the operating principle of alloys and alloy interlayers is still not well understood.[43] For long-term operation conditions, there is strong experimental and theoretical evidence that these interlayers do not necessarily remain located at the interface and may not improve the anode kinetics in the long term.[24,39,41,42] Thus one must assume that most of the interlayers mainly act as contact mediator during cell assembly and new solutions need to be found to address and circumvent the vacancy diffusion limitation of lithium metal anodes.

Yang et al.[44] recently investigated Li–Mg alloys as alternative to bare lithium metal on LLZO type garnet electrolytes with very promising performance. However, the kinetics inside the alloy electrode itself is not understood in detail. Clearly, in addition to the different wetting behavior the alloying will highly affect lithium diffusion and the limiting current density.

The phase diagram of Li–Mg is shown in **Figure 1**a. A unique feature of the phase diagram is the wide solubility range of magnesium in lithium. Up to around 70 at% of magnesium can be dissolved in lithium before a phase transition from the β- to the α-phase occurs. Additionally, there are literature reports that suggest a very high lithium diffusion coefficient of the β-phase of up to $D(\mathrm{Li}) \approx 10^{-7}$ cm² s^{-1}, which is the key ingredient to the better transport kinetics inside the alloy anode. The theoretical gravimetric and volumetric capacity of lithium in a representative $Li_{0.9}Mg_{0.1}$ alloy is 2820 mAh g^{-1} and 1870 mAh cm^{-3}, respectively, which is close enough to pure lithium metal with 3860 mAh g^{-1} and 2060 mAh cm^{-3} to be of practical interest. Even if the lithium in a remaining α-phase cannot be addressed during cycling, the values are as high as 1850 mAh g^{-1} and 1220 mAh cm^{-3}, which are still much higher compared to commonly used graphite anodes (350 mAh g^{-1} and 760 mAh cm^{-3}). Combined with a very low potential close to the potential of the pure lithium metal anode (see Figure S1, Supporting Information), high energy densities can be theoretically achieved, making the Li–Mg alloy an attractive anode material compared to other alloys.[45] In liquid electrolytes, poor rate capabilities have been reported for Li–Mg alloy electrodes that, combined with the low potential, can lead to lithium plating during charge and the danger of short circuiting due to dendrite growth through the liquid electrolyte.[46,47] However, recently enhanced performance compared to bare lithium electrodes was shown mainly because of morphological stability of the alloy during discharge.[48]

In solid-state batteries, the retained structural rigidity and morphological stability will have an even greater influence, as morphologically unstable anodes (such as pure lithium anodes) can hardly operate without high external pressure. Overall, the distinctive diffusion characteristics compared to bare lithium metal electrodes may have highly beneficial effects. However, a detailed comparison between the rate capability of lithium and a Li–Mg alloy in SSBs is still missing.

This work aims to fill this gap and investigate in detail the diffusion limitations of lithium and Li–Mg alloy anode and its effect on the solid|solid interface as a function of temperature and pressure. Operando galvanostatic electrochemical impedance spectroscopy (GEIS) stripping experiments on Li, $Li_{0.95}Mg_{0.05}$, and $Li_{0.9}Mg_{0.1}$ model electrodes were performed to investigate the effect of Mg-alloying on the morphological changes at the interface. In combination with electron microscopic investigations (ex situ), this work shows that macroscopic pore formation can be effectively eliminated by alloying. However, it also shows that a diffusion controlled delithiation limitation exists for the alloy. Based on these experimental findings, a quantitative diffusion model for a representative

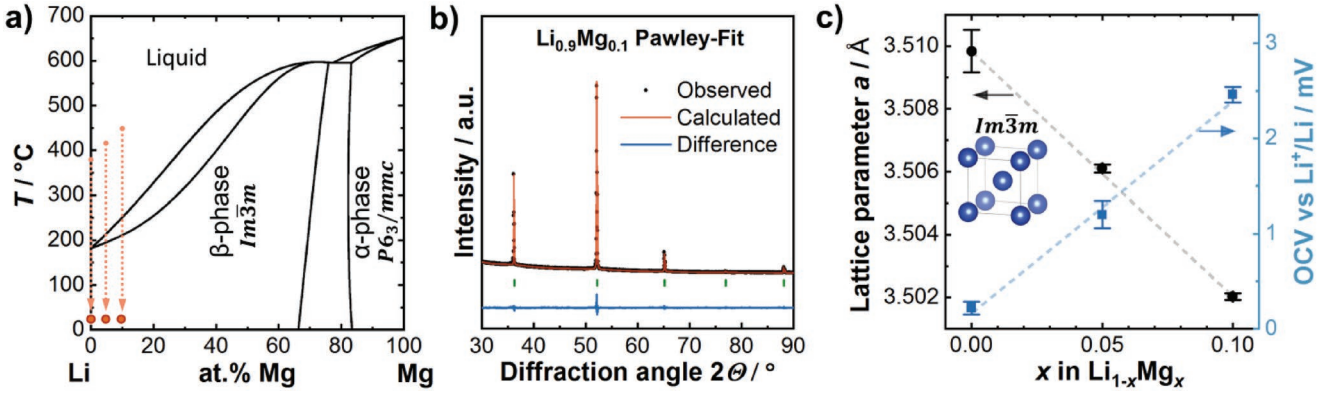

Figure 1. a) Phase diagram of the binary Li–Mg system. Data digitized from Kevorkov et al.[53] The red dots represent the compositions analyzed in this study and the arrows indicate the thermal history during the synthesis of the alloy compositions. b) Representative X-ray diffraction data and result of a Pawley-Fit of $Li_{0.9}Mg_{0.1}$. Experimental data are shown as points; the red line denotes the calculated pattern, and the difference profile is shown in blue. Calculated positions of Bragg reflections are shown by green vertical tick marks. c) The lattice parameter of the Li–Mg alloys shows a linear decrease, while the open circuit potential versus Li$^+$/Li increases linearly with increasing magnesium fraction. The error bars of the OCV reflect the standard deviation of the measured values (see Table S1, Supporting Information).

$Li_{0.9}Mg_{0.1}$ alloy electrode is proposed, which allows screening the rate capability for practical applications without the need for time consuming experiments.

2. Results

2.1. Alloy Characterization

Two Li–Mg alloy compositions, namely $Li_{0.95}Mg_{0.05}$ and $Li_{0.9}Mg_{0.1}$, were synthesized. Both are in the solid solution range of the β-phase, which exists over a stoichiometry window of 0–69 at% Mg at room temperature (see Figure 1a). Figure 1b shows an exemplary diffraction pattern as well as the result of a Pawley fit for the composition $Li_{0.9}Mg_{0.1}$. The other refinements as well as the fit residuals can be found in Figure S2 in the Supporting Information. All diffraction patterns could be indexed to the β-phase, crystallizing in the $Im\bar{3}m$ space group (no. 229). The refined lattice parameters (see Figure 1c) show a linear decrease from 3.5098(6) to 3.5020(1) Å upon substituting 10 at% Li by Mg in excellent agreement with literature values,[49–51] confirming the successful synthesis of the alloy phases. It has to be noted that a strong texturing of the alloy anodes is observed due to anisotropic crystal orientation distribution caused by to the pressing protocol.

The open circuit voltage (OCV) of the alloys versus Li^+/Li was measured in $Li/LLZO/Li_{1-0.x}Mg_{0.x}$ cells. Figure 1c shows a linear increase of the OCV according to $OCV = 2.5\ mV \cdot x$ ($Li_{1-0.x}Mg_{0.x}$). For a larger compositional range of the α and β-phase, the OCV dependence at room temperature is shown in Figure S1 in the Supporting Information. It was calculated for room temperature using the activity coefficients γ_{Li} reported by Iwadate et al.[52]

2.2. Operando Stripping Experiments

GEIS was performed to measure the temporal evolution of the impedance during anodic load. Therefore, 100 µm thick Li and Li–Mg alloy anodes were anodized at 100 µA cm^{-2} until full depletion of lithium at the interface has occurred. The time until full the depletion is observed is denoted in the following as depletion time t_0. **Figure 2**a shows the potential profiles during anodic dissolution. The $Li_{0.9}Mg_{0.1}$ alloy shows an increase of the depletion time from 9 h to around 15 h.

When attaching the working electrodes at a high pressure of 400 MPa, the initial interface resistance becomes negligibly small for both Li and $Li_{0.9}Mg_{0.1}$. The overpotential evolution of these ideally contacted working electrodes behaves differently (see dotted lines in Figure 2a). A strong increase of the potential takes place only in the end. Nevertheless, the depletion times of the more strongly pressed electrodes $\tilde{t}_0$ area almost identical to the depletion times t_0 of the more gently pressed electrodes with higher initial interface resistance, for both lithium and the Li–Mg alloy. The reason for this is that the global current density and thus the lithium transport in the bulk lithium and lithium alloy electrode seem to be not highly affected by the initial interface resistance. In the following studies, measurements with a high initial interface resistance are preferred as changes in the impedance can be detected, which would be invisible for a negligibly small initial interface resistance. As the DC characteristics alone do not reveal the mechanisms that are responsible for the different depletion times, the operando recorded impedance spectra need to be evaluated.

Figure 2d,e shows the impedance evolution in a Bode type phase angle versus frequency plot for a lithium metal and a $Li_{0.9}Mg_{0.1}$ alloy working electrode, respectively. The corresponding Nyquist Plots can be found in Figure S3 in the Supporting Information. Three impedance contributions can be separated. These can be assigned to bulk transport, grain boundary charge transfer, and an interface process.[26] The bulk transport ($\omega_{max} \approx 40$ MHz) and the grain boundary charge transfer ($\omega_{max} \approx 600$ kHz) contributions do not change with time, indicating the absence of lithium metal penetration through the solid electrolyte.[24] This was observed for all measurements in this study and corroborates the absence of soft short circuits. However, there are distinctive differences in the evolution of the interface resistance contribution between bare lithium and the $Li_{0.9}Mg_{0.1}$ alloy electrode.

Figure S4 in the Supporting Information shows the fitted interface resistance and capacitance values. The interface resistance increases for both, the lithium metal and the Li–Mg alloy electrode, but the increase is delayed in case of the $Li_{0.9}Mg_{0.1}$ alloy. This means that the depletion of the number of active sites at the interface is slowed down in the Li–Mg alloy, which suggests faster lithium transport inside the electrode that is counteracting the depletion of lithium. More importantly, the evolution of the interface capacitance shows different behaviors of the lithium metal and the Li–Mg alloy electrode. While a linear decrease is found for lithium, the interface capacitance remains high for the Li–Mg alloy and decreases only at the end of the stripping process. Figure 2b shows the data of Figure S4 in the Supporting Information but with a normalization of the capacity-axis. The interface resistance evolution is nearly overlapping and a similar diffusive transport mechanism may be assumed. However, the clearly different slope of the interface capacitance suggests a completely different mechanism of anodic lithium dissolution. While the interface capacitance drops to 2% of the initial value for the lithium metal, the interface capacitance of the $Li_{0.9}Mg_{0.1}$ alloy at t_0 is still 40% of the initial value. This observation suggests less morphological instability for the $Li_{0.9}Mg_{0.1}$ alloy as schematically shown in Figure 2c. To further investigate this effect, the working electrodes were delaminated after achieving the electrochemical delithiation and the sides facing the solid electrolyte were investigated using scanning electron microscopy. While the bare lithium electrode could be easily removed from the garnet pellet, the adhesion of the Li–Mg alloy was still strong and delamination was more difficult. Visual inspection showed that the Li foil was roughened, while the Li–Mg alloy electrode was still shiny (see Figure S5, Supporting Information). **Figure 3**a shows the morphology of the lithium metal anode at the interface on the micro- and sub-micrometer scale. As can be seen, large pores (in the µm scale) have formed on the lithium metal electrode and only a small area of the lithium metal was in contact with the solid electrolyte after stripping. This is in good agreement with the interface capacitance that suggests a contact loss of 98% compared to the initial contact area. For the Li–Mg alloy, however, no large pores were found and the full alloy area

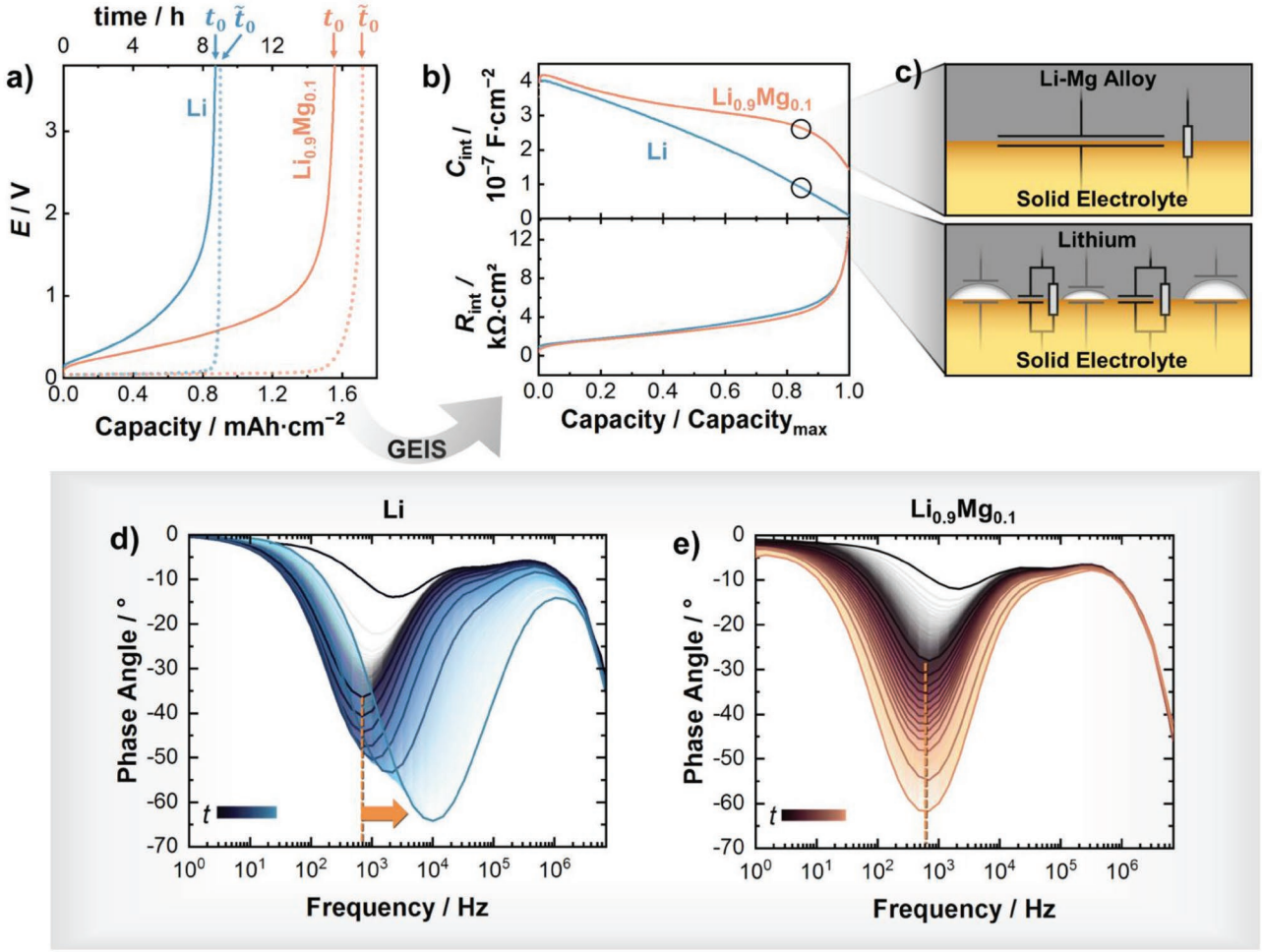

Figure 2. Results of operando stripping experiments of Li and Li–Mg alloy electrodes. a) Potential profile during stripping at $i = 100$ µA cm^{-2}. The potential profile of lithium is shown as a solid blue line for an initial interface resistance value of 0.3 kΩcm² and for an ideally contacted lithium metal electrode with an interface resistance value of 0 Ωcm² as blue dotted line. For the $Li_{0.9}Mg_{0.1}$ alloy it is shown in orange, respectively. Despite the very different initial interface resistances, similar depletion times were obtained. b) Evolution of the interface resistances R_{int} and interface capacitances C_{int} obtained from the evaluation of the impedance spectra is shown against the normalized capacity. For the $Li_{0.9}Mg_{0.1}$ alloy the interface capacitance remains high while for Li it continuously drops. The continuous decrease for bare lithium can be traced back to pore formation at the interface during Li stripping that is strongly reduced in the Li–Mg alloy as schematically shown in (c). The impedance spectra in a Bode type phase angle versus frequency plot are shown in (d) and (e) for lithium and the $Li_{0.9}Mg_{0.1}$ alloy, respectively.

seems to have still been in contact with the garnet even after full delithiation. Nevertheless, on the sub-micrometer scale, pores can be found (see inset in Figure 3b). The contact area of 40% estimated from the interface capacitance agrees well with the remaining contact estimated from the scanning electron microscope (SEM) analysis.

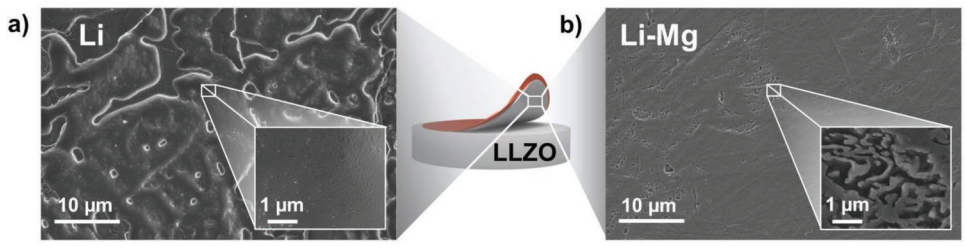

Figure 3. SEM images showing the morphology of a) the lithium and b) Li–Mg alloy electrode after stripping experiments at $i = 100$ µA cm^{-2}. Large pores and nearly full contact loss were observed for the bare lithium electrode, while for the Li–Mg alloy only pore formation takes place on the sub-micrometer scale resulting in maintained contact even after full lithium depletion at the interface. The relatively smooth surface (inset in (a)) of the large pores can be attributed to the high surface tension of pure lithium metal.

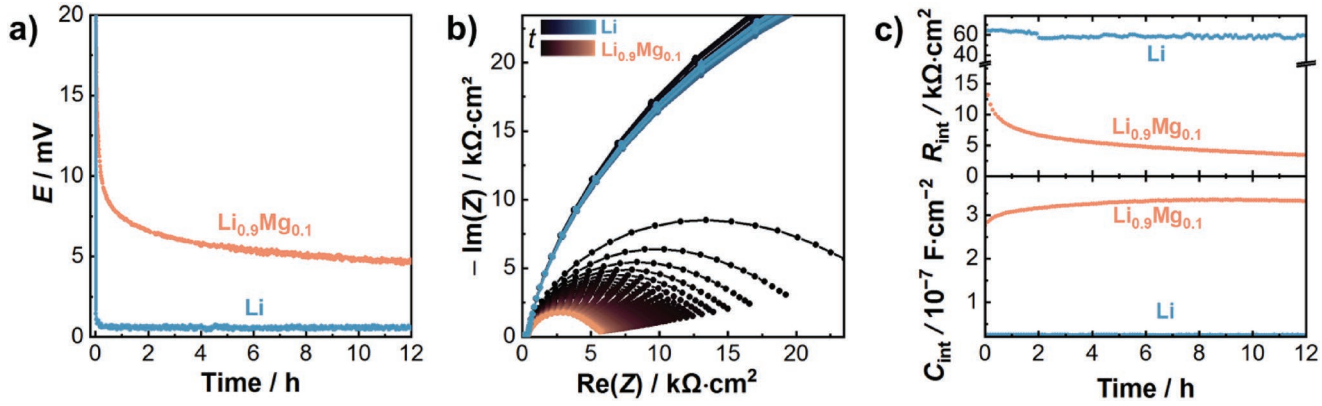

Figure 4. a) OCV decay after a lithium stripping experiment at $i = 100$ µA cm^{-2} after the cutoff potential of 4 V is reached. b) Nyquist representation of the evolution of the impedance spectra during the OCV and c) interface resistance and interface capacitance evolution during the OCV.

To further validate the effects of the quite different morphological evolution, relaxation experiments were performed. Therefore, the OCV as well as the impedance were immediately recorded after the electrodissolution (stripping) experiments at 100 µA cm^{-2}. **Figure 4**a shows the OCV decay for Li and $Li_{0.9}Mg_{0.1}$. While the OCV for the lithium metal drops immediately to around 0 mV, the OCV for the $Li_{0.9}Mg_{0.1}$ alloy decreases slowly to 4.5 mV after around 12 h. Ex situ X-ray diffraction of a delithiated Li–Mg alloy electrode (see Figure S6, Supporting Information) confirms that no irreversible α-phase formation takes place during the performed stripping experiments; however, the lattice parameter decreases to 3.5005(1) Å, which corresponds to an alloy composition of $Li_{0.88}Mg_{0.12}$ (see Figure 1c). Simultaneously with the increase of the lithium concentration at the interface, the interface resistance decreases, whereas the interface capacitance remains almost constant (see Figure 4b,c). This corroborates that for the Li–Mg alloy not only the contact loss, but predominantly the decrease in the lithium concentration at the interface region of the alloy is responsible for the increase of the interface resistance during stripping. In contrast, for the bare lithium metal the interface resistance remains constantly high without significant relaxation. This demonstrates that the morphological changes are irreversible when no external pressure is applied.

In the following, important parameters and their influence on the (anodic) rate capability of a lithium metal anode on solid electrolytes are tested. In detail, we show current density, pressure, and temperature-dependent measurements of both Li–Mg alloy and lithium metal electrodes.

2.3. Current Density Dependence

Figure 5a shows potential profiles of Li, $Li_{0.95}Mg_{0.05}$, and $Li_{0.9}Mg_{0.1}$ electrodes during delithiation at 50, 100, and 200 µA cm^{-2}. Here, a higher current density leads to faster depletion of lithium at the interface (i.e., smaller depletion times t_0). For all current densities, the depletion time t_0 of the $Li_{0.9}Mg_{0.1}$ alloy is around a factor of two higher than for the bare lithium electrode. The $Li_{0.95}Mg_{0.05}$ alloy has a minimally lower depletion time than the $Li_{0.9}Mg_{0.1}$ alloy. For a more detailed comparison, the interface resistance estimated from the impedance response of the GEIS measurements is plotted against the areal capacity (see Figure 5b). It clearly demonstrates that lithium depletion occurs faster for higher current densities in

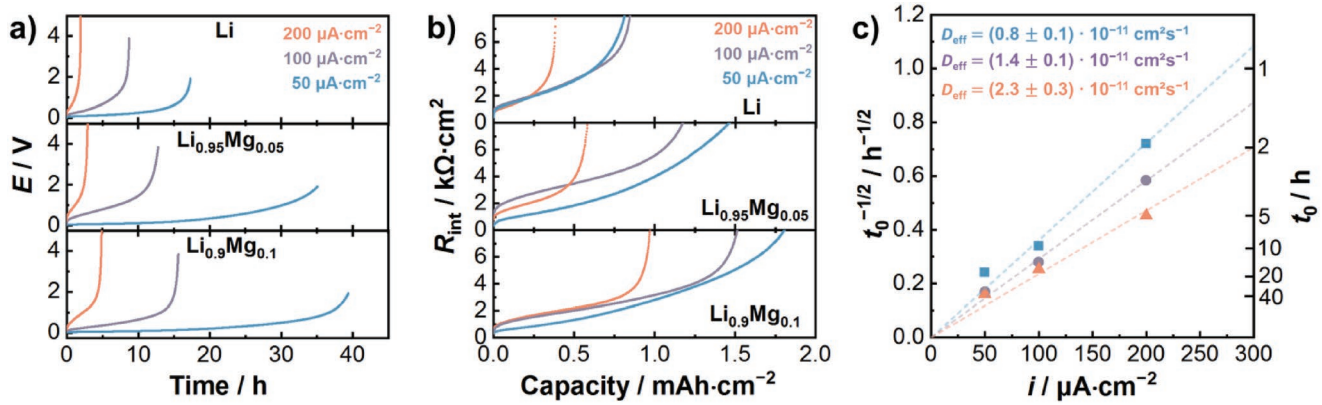

Figure 5. Results of current-dependent delithiation experiments of Li and Li–Mg alloy electrodes. a) Time-dependent potential profiles show a strong decrease of the depletion time t_0 with increasing current density. In (b) the extracted interface resistances are shown in relation to the areal capacity. In (c) the delithiation current density and depletion time dependence ($t_0^{-1/2}$ vs i) are shown according to Sand's equation, which was used for the estimation of lithium diffusion coefficient.

all electrode types. This suggests that for all electrodes, there has to be a transport mechanism in the electrode that counteracts lithium loss. For a detailed overview of the mechanism governing contact loss for a pure lithium metal electrode, we like to refer to previous work.[26] Figure S7 in the Supporting Information shows the trend of the interface capacitances. While the interface capacitance drops to almost zero due to full contact loss, it remains high for the $Li_{0.9}Mg_{0.1}$ alloy. The $Li_{0.95}Mg_{0.05}$ alloy shows an intermediate behavior. This indicates that an initial atomic fraction of 5% Mg in the alloy is not high enough to effectively prevent pore formation. Figure S8 in the Supporting Information shows the interface structure of the lithium and alloy electrodes after full delithiation at 50 and 200 μA cm^{-2}. Indeed, $Li_{0.95}Mg_{0.05}$ also shows pores that are, however, not as pronounced as for the pure lithium electrode. The $Li_{0.9}Mg_{0.1}$ alloy electrodes do not show macroscopic pores at any of the applied current densities.

Assuming a classical chemical diffusion process driven by the lithium concentration gradient in the alloy, one can determine effective diffusion coefficients of lithium (D_{eff}) in the electrode based on the depletion times t_0. Because of the fulfilled assumption $t_0 \ll L^2 \cdot D_{eff}^{-1}$ in which L denotes the electrode thickness, Sand's equation[54] can be used for the estimation (neglecting interface kinetics)

$$\frac{1}{\sqrt{t_0}} = \frac{2}{\sqrt{D_{eff} \cdot \pi} \cdot c_0 \cdot F} \cdot i \tag{1}$$

Herein, c_0 denotes the initial concentration of lithium that is—based on the refined lattice parameters—76.8, 73.2, and 69.6 mmol cm^{-3} for Li, $Li_{0.95}Mg_{0.05}$, and $Li_{0.9}Mg_{0.1}$, respectively. For t_0, we adopt the time values, when the interface resistance exceeds a value of 10 kΩ, which is equivalent to nearly full depletion of lithium at the interface. A similar procedure was already performed by Jow and Liang to estimate the lithium diffusion coefficient of a bare lithium metal electrode on a solid electrolyte.[32] Figure 5c shows a plot of $t_0^{-1/2}$ versus i. From the slope, the apparent diffusivity of Li can be estimated. The effective diffusion coefficient D_{eff} increases with increasing Mg content from $D_{eff} = 0.8 \times 10^{-11}$, 1.4×10^{-11} to 2.3×10^{-11} cm^2 s^{-1} for Li, $Li_{0.95}Mg_{0.05}$ and $Li_{0.9}Mg_{0.1}$, respectively. With a similar experiment, Jow and Liang estimated a diffusion coefficient for pure Li of $(5.6 \pm 0.9) \times 10^{-11}$ cm^2 s^{-1}.[32] A strong impact of the preparation protocol (i.e., the thermal and mechanical "history") of the lithium metal on the diffusion properties is expected. It is likely that the different density of nonequilibrium lattice defects (i.e., dislocations and grain boundaries), which are known as fast-diffusion pathways in metals, are responsible for the observed spread.[55–57] By heating a lithium metal working electrode for 3 h to 10 K below the melting point, the depletion time at 100 μA cm^{-2} reduces to 3.5 h (see Figure S9, Supporting Information), probably because of the decrease in the dislocation density during annealing. This also shows the impact of the thermal history as well as of impurities that can, in principle, also severely enhance or decrease the rate capability of the lithium metal anode on solid electrolytes. A strong interrelationship between nonequilibrium defects and the electrodissolution behavior was already proven for silver and copper electrodes.[58]

The herein estimated diffusion coefficients are therefore denoted as effective diffusion coefficients. They should not be confused as a lattice or self-diffusion coefficient (D_{Li}) evaluated from other experiment methods like spin relaxation measurements in which values in the range of $(7 \pm 2) \times 10^{-11}$ cm^2 s^{-1} have been determined (see Table S2 in the Supporting Information for a detailed overview). The herein estimated diffusion coefficients are dependent on the concentration of nonequilibrium defects as well as the morphological instability of the interface, which leads to a complicated 3D diffusion problem in which surface (adatom) diffusion is significantly involved.[55] Nevertheless, D_{eff} is a valuable practical kinetic parameter that gives insights into the rate capability of the anode at a solid|solid interface. For the $Li_{0.9}Mg_{0.1}$ alloy, D_{eff} can be almost interpreted as average chemical diffusion coefficient $\tilde{D}_{Li}$, as the morphological change of the interface is less pronounced. In a following section, we show a more detailed analysis of the diffusion properties of Li–Mg alloy electrodes.

2.4. Temperature Dependence

Vacancy diffusion, adatom diffusion, and chemical diffusion are activated processes; therefore, an exponential temperature dependence is expected for the depletion times t_0 according to Equation (2) in which E_A denotes the activation energy for diffusion that consists of both, the enthalpy of vacancy formation and vacancy migration.

$$D = D_0 \cdot e^{-\frac{E_A}{kT}} \tag{2}$$

To evaluate the temperature dependence, Li and $Li_{0.9}Mg_{0.1}$ electrodes were delithiated/stripped at 0, 25, and 50 °C without external pressure (atmospheric pressure). **Figure 6**a shows the potential evolution for stripping experiments at 100 μA cm^{-2}. At 0 °C the potential increase is much faster than for room temperature and for 50 °C even after 25 h no full depletion of the lithium at the interface can be observed.

To compare the degree of lithium depletion at the interface for the different temperatures, R_{int} values were normalized according to Equation (3)

$$R_{int}(T_0) = \frac{T_0}{\frac{T}{R_{int}(T)} \cdot e^{-\frac{E_A}{R}\left(\frac{1}{T_0} - \frac{1}{T}\right)}} \tag{3}$$

where T is the temperature at which the measurement was performed, T_0 is room temperature, and E_A is the activation energy for the interface process. The activation energy was measured by temperature-dependent impedance spectroscopy for cells with an interface resistance of 0.3 kΩ cm^2 (see Figure S10, Supporting Information). As in a previous work, the average activation barrier was 0.37 eV, and no significant difference was observed between the alloy and lithium metal electrode. This is because the activation energy is mainly determined by migration in the solid electrolyte in the constriction zone.[26] Figure 6b shows that the lithium depletion takes place more rapidly at lower temperatures. For Li, this

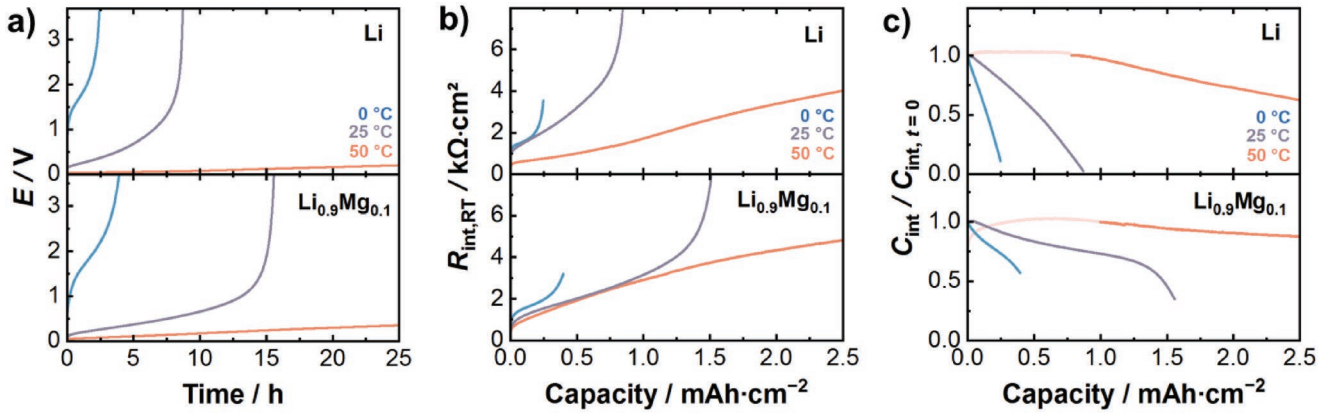

Figure 6. Temperature-dependent delithiation/stripping experiments at $i = 100$ µA cm^{-2} and at 0, 25, and 50 °C. a) Potential profile for a Li and $Li_{0.9}Mg_{0.1}$ electrode. In (b) the interface resistance evolution was normalized according to Equation (3), to have a direct comparison of the depletion of lithium at the interface. In (c) the interface capacitances, normalized to their initial value after assembly are shown for the different temperatures.

can also be seen in a much faster decay of the interface capacitance (see Figure 6c). According to Equation (1) one can determine $\tilde{D}_{Li}$ for 0 °C. At 0 °C, the lithium diffusivity is estimated to $\tilde{D}_{Li} \approx 5.0 \times 10^{-12}$ cm^2 s^{-1} and $\tilde{D}_{Li} \approx 2.6 \times 10^{-12}$ cm^2 s^{-1} for $Li_{0.9}Mg_{0.9}$ and Li, respectively. At 50 °C, full depletion cannot be detected even after a flown charge of 2.5 mAh cm^{-2}. This shows experimentally that the temperature has a very strong effect on the lithium diffusion properties as well as on the morphological stability. Slightly higher temperatures than room temperature might be quite beneficial for the operation of lithium metal and Li–Mg alloy electrodes.

2.5. Pressure Dependence

In a previous work, our group was able to demonstrate the strong pressure dependence of the interface under current load for lithium metal and showed that with a stack pressure of 35 MPa, pore growth can be effectively prevented at 100 µA cm^{-2}.[26] Recent work by Wang et al. demonstrates that a critical stack pressure can be defined, at which the rate of pore formation in lithium metal due to anodic load can be balanced by the rate of pore annihilation due to creep and it was observed that this pressure can quickly exceed the MPa range for high current densities over 100 µA cm^{-2}.[28]

Since the morphological changes during dissolution are drastically different for lithium and the Li–Mg alloy electrodes, the pressure dependence needs to be investigated. **Figure 7**a shows potential profiles during stripping at a current density of 200 µA cm^{-2} under different pressures. For a lithium metal electrode, the potential increase can be clearly reduced by external pressure. Full contact loss at 200 µA cm^{-2} can already be mitigated at a pressure of 3.8 MPa. At 15 MPa, there is already no major change in the interface resistance visible (see Figure 7b). The maintained contact can also be seen in the evolution of the interface capacitances. While the capacities decrease very quickly without externally applied pressure, they drop much slower with external load and a steady state is reached, when the rate of pore annihilation due to plastic deformation reaches the rate of pore formation due to the external applied current. The slight increase of the interface capacitance at 15 MPa can be assigned to a small increase of the lithium metal anode diameter due to plastic deformation.

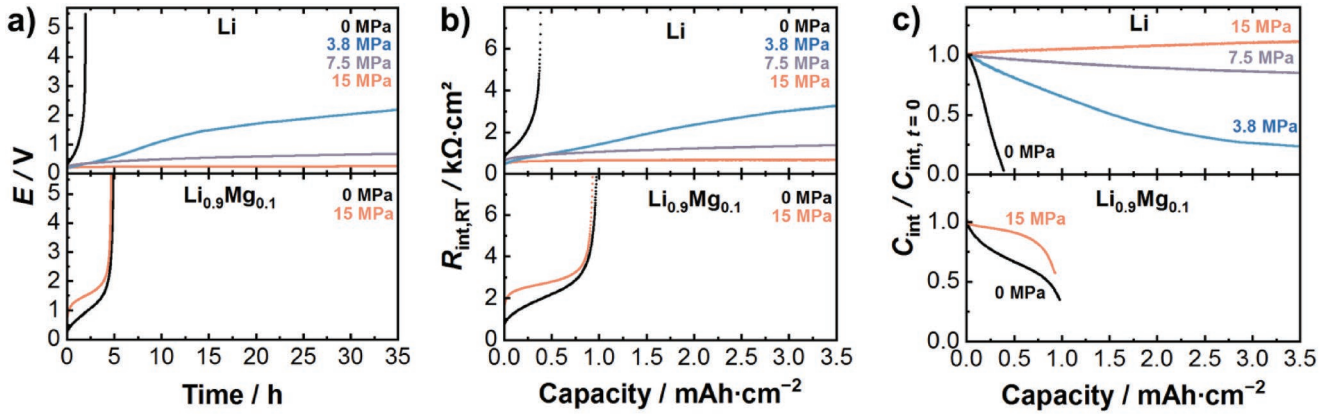

Figure 7. Pressure-dependent delithiation experiments at $i = 200$ µA cm^{-2} at 0, 3.8, 7.5, and 15 MPa. a) Potential profile for a Li and $Li_{0.9}Mg_{0.1}$ electrode. In (b), the interface resistance evolution is shown. (c) shows the interface capacitances, normalized to their initial value after assembly.

In stark contrast, the depletion time t_0 for the Li–Mg alloy is not significantly affected by external pressure. External load obviously has no large impact on the lithium depletion mechanism. This can be traced back to the different depletion mechanisms taking place during stripping. For lithium, pores in the microscale are formed, which can be easily annihilated by plastic deformation due to dislocation movement upon external pressure. However, for the Li–Mg alloy the depletion of the lithium concentration in the alloy is responsible for the increase in overvoltage. The sub-micrometer scale pores that are forming on the Li–Mg alloy at higher depletion levels cannot be annihilated by the external pressure of 15 MPa as can be seen in Figure 7c at the changing slope of the interface capacitance after a flown charge of around 0.7 mAh cm^{-2}. Additionally the increasing Mg concentration at the interface also leads to locally higher elastic constants,[59] which further hinders plastic deformation. In summary, external pressures in the low MPa range cannot enhance the interface kinetics of a Li–Mg alloy. Combined with the results obtained for the temperature-dependent diffusion properties, a very strong coupling between temperature and pressure effects is expected for bare lithium metal anodes. Not only lithium diffusion in the metal anode is exponentially increased with rising temperature, also the diffusion driven creep, which is important for the pore annihilation mechanism, shows an exponential dependence on temperature.[28,60,61] The homologous temperature may be a good descriptor for the combined temperature and pressure dependency of the cycling behavior. The homologous temperature $T_H = T \cdot T_{mp}^{-1}$, in which T_{mp} denotes the melting temperature of the Li–Mg alloy, decreases with increasing Mg content as can be seen in the binary phase diagram (see Figure 1a) and decreases the rate of diffusion dependent deformation. This shows that there is a complicated but very strong temperature influence on the dissolution under applied stack pressures, which has to be taken into account for practical applications.

2.6. Influence on the Critical Current Density and the Cycling Behavior

The work above shows the influence of alloying lithium metal with Mg on the kinetics of the interface under anodic load. However, for fast charging the cathodic rate capability of the lithium metal anode is of great interest. To explore whether the alloying with Mg also reduces the lithium penetration susceptibility, critical current density (CCD) tests were performed with Li and Li–Mg alloy electrodes that were contacted at 400 MPa external pressure to form an ideal interface. For both setups, no interface resistance can be detected in the resolution limit of potentiostatic electrochemical impedance spectroscopy (PEIS) (<2 Ωcm^2). This enables a fair comparison of the effect of alloying, as the same load bearing contact area can be expected. Figure S11a,b in the Supporting Information shows the CCD tests for Li and $Li_{0.9}Mg_{0.1}$, respectively. For both electrode types, the CCD is in the range between 200 and 300 μA cm^{-2}. There is no beneficial effect on the CCD by using the Li–Mg alloy. This can be well understood, as the activity of lithium is changed only to a small extent by alloying with 10% of Mg. For well contacted lithium metal anodes and the solid electrolyte of the composition $Li_{6.25}Al_{0.25}La_3Zr_2O_{12}$, a value of 300 μA cm^{-2} was widely found as CCD at room temperature.[27,62]

However, as the CCD will highly depend on the current distribution and thus the interfacial contact, plating/stripping experiments should benefit from the maintained contact of the Li–Mg alloy. Figure S12 in the Supporting Information shows a cycling experiment with intentionally badly contacted electrodes. Indeed, for the lithium electrode, where the interface resistance increase is dominated by contact loss, a short circuit can already be found directly after plating on the anodically deteriorated electrode. For the Li–Mg alloy, no short circuit is observed and the interface resistance vanishes quickly during cathodic load. These results clearly show that the maintained contact for the Li–Mg alloy is highly beneficial for stable cycling if no external pressure is applied. Current constriction due to pore formation and growth can be effectively mitigated. This is especially important, when a high charge is passed, which is required under realistic conditions or in practice.

3. Discussion

The work elucidates fundamental differences in the delithiation/stripping kinetics between lithium metal and lithium rich Li–Mg alloy anodes on LLZO solid electrolyte. In the following a kinetic model that predicts the rate capability of the Li–Mg alloy anode is proposed, which may support future battery cell development. In a bare lithium metal anode, the change of the interface resistance is solely influenced by morphological changes; in particular by macroscopic pore formation on the microscale at the interface. Thus for modeling, a 3D microkinetic diffusion model, which includes hardly accessible adatom diffusion processes on pore walls, is required (see **Figure 8**a). A suitable kinetic model combining volume and surface diffusion is unfortunately beyond the scope of this study. However, for the Li–Mg alloy a comparably simple 1D model of chemical diffusion obeying Fick's 2nd law is—with a few limitations—applicable, if we neglect the structural changes of the interface on the sub-micrometer scale (see Figure 8b). This assumption can be considered as justified, since the morphological changes are much less pronounced as experimentally confirmed (see above).

3.1. Diffusion Model of the Li–Mg Alloy

A detailed kinetic diffusion model for delithiation of Li–Mg alloy electrodes in liquid electrolytes was already reported by Zhang et al.[63] However, in the case of a solid–solid interface a different treatment of the problem with different assumptions is required. Here, only the diffusion processes in the β-phase needs to be taken into account because the α-phase has a several order of magnitude lower diffusivity.[52] Further, the observed sub-micrometer scale pore formation after segregation of the α-phase will not lead to enhanced delithiation kinetics as a solid|solid interface cannot compensate contact through wetting like in a liquid electrolyte. Thus, the depletion of the lithium concentration at the interface after formation of the α-phase is assumed to be very fast and can hence be neglected.

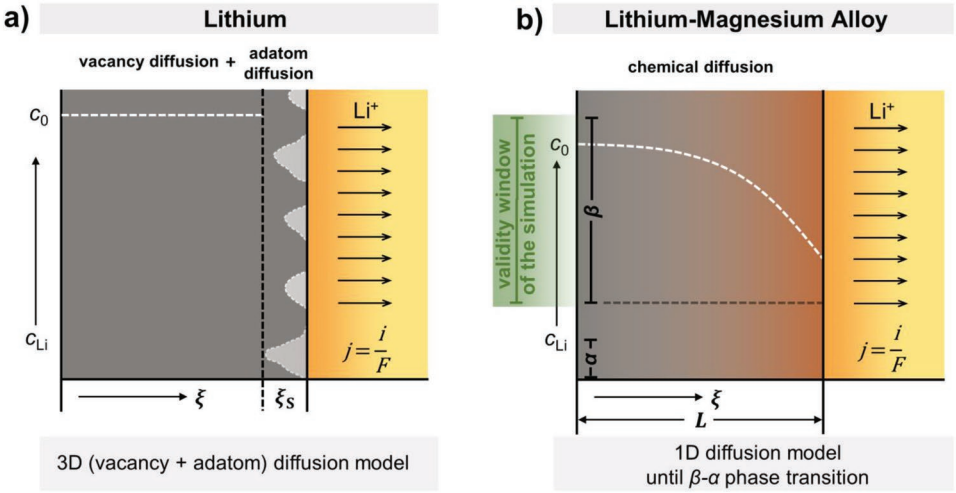

Figure 8. Schematic summarizing the lithium transport properties as well as the morphological change of the interface for a) a lithium metal electrode and b) a Li rich Li–Mg alloy electrode during anodic load. ξ denotes the distance from the nonactive electrode side, c_{Li} the lithium concentration in the alloy or in the lithium metal and L denotes the alloy thickness. ξ_S is the structural relaxation zone in lithium metal caused by nonequilibrium defects as pores.

The delithiation process can thus be modeled based on Fick's 2nd law in the validity range of the β-phase (c_{Li} = 24.0–69.6 mmol cm^{-3}):

$$\frac{\partial c_\beta(\xi,t)}{\partial t} = \tilde{D}_\beta \cdot \frac{\partial^2 c_\beta(\xi,t)}{\partial \xi^2} \tag{4}$$

Dependent on the delithiation current density i, the time-dependent concentration profiles of the Li–Mg model electrode can be obtained according to Equation (5).[63]

$$c_\beta(\xi,t) = c_0 + \frac{iL}{6\tilde{D}_\beta F} - \frac{i}{FL}\cdot t - \frac{i}{2\tilde{D}_\beta FL}\xi^2 + \frac{2jL}{\tilde{D}_\beta F\pi^2}\sum_{n=1}^{\infty}\frac{(-1)^n}{n}\cos\left(\frac{n\cdot\pi}{L}\xi\right)\cdot\exp\left(-\frac{n^2\cdot\pi^2}{L^2}\tilde{D}_\beta\cdot\xi\right) \tag{5}$$

Based on our experimentally derived depletion times t_0 of the β-phase, a diffusion coefficient of $\tilde{D}_\beta = 3\times10^{-11}$ cm^2 s^{-1} can be estimated, which is in reasonable agreement with the value estimated by neutron tomography by Zhang et al. ($\tilde{D}_\beta = 6\times10^{-11}$ cm^2 s^{-1}).[63] It has to be noted that literature data for the lithium diffusion coefficients of the β-phase are inconsistent (see Table S2, Supporting Information), with very high reported values up to $D_\beta = 10^{-7}$ cm² s^{-1} which would suggest very fast delithiation kinetics. We assume that these reported values are apparent diffusion coefficients that do not correlate with bulk (lattice) diffusion but rather reflect fast surface, grain boundary, or dislocation diffusion processes and are highly dependent on the effective surface area. For accessing the high theoretical capacity of the anode material, these values are, however, not representative as the diffusive transport for long time stripping experiments are ultimately limited by diffusion through the bulk, even if the overall transport might be aided by boundary diffusion processes. In the measurements above, the grain size of the alloy was found to be larger than 20 µm (see Figure S13, Supporting Information). Thus, it is justified to assume that the effect of grain boundary diffusion does not contribute largely to the overall diffusion and that the measurements rather reflect bulk diffusion.

With the obtained average diffusion coefficient, concentration profiles can now be simulated for different boundary conditions. For the simulation, we used the finite element method (FEM) because the analytical solution of Equation (5) has a boundary value problem. The boundary conditions and assumptions used for this model as well as their validation based on our experiments can be found in detail in Table S3 and Figure S14 in the Supporting Information.

3.2. Estimation of Anode Utilization as a Function of Temperature

For practical applications, at least an area specific capacity of 5 mAh cm^{-2} needs to be stripped.[31] This corresponds to a $Li_{0.9}Mg_{0.1}$ alloy thickness of around 25 µm (26.7 µm). **Figure 9** shows time-dependent simulations performed for these alloy anode thicknesses at current densities of 10 µA cm^{-2}, 100 µA cm^{-2}, and 1 mA cm^{-2}, before unwanted precipitation of the α-phase starts.

With help of the simulation, the utilization of lithium in the anode during continuous discharge at 10 µA cm^{-2}, 100 µA cm^{-2}, and 1 mA cm^{-2} can now be estimated, which is 61%, 27%, and 6%, respectively. The estimated values only reflect a lower limit because the stripping after formation of the α-phase was not considered herein, which will further contribute to higher capacities. The utilization neglecting the lithium trapped in the α-phase, herein denoted as "Li utilization (β-phase)." is a better descriptor for the rate capability and is 93%, 41%, and 9%, at 10 µA cm^{-2}, 100 µA cm^{-2}, and 1 mA cm^{-2}, respectively.

Overall, the simulations clearly demonstrate that at room temperature, planar bulk Li–Mg alloy anodes with an average chemical lithium diffusion coefficient of $\tilde{D}_{Li} = 3\times10^{-11}$ cm² cannot be used for fast charge capable solid state batteries.

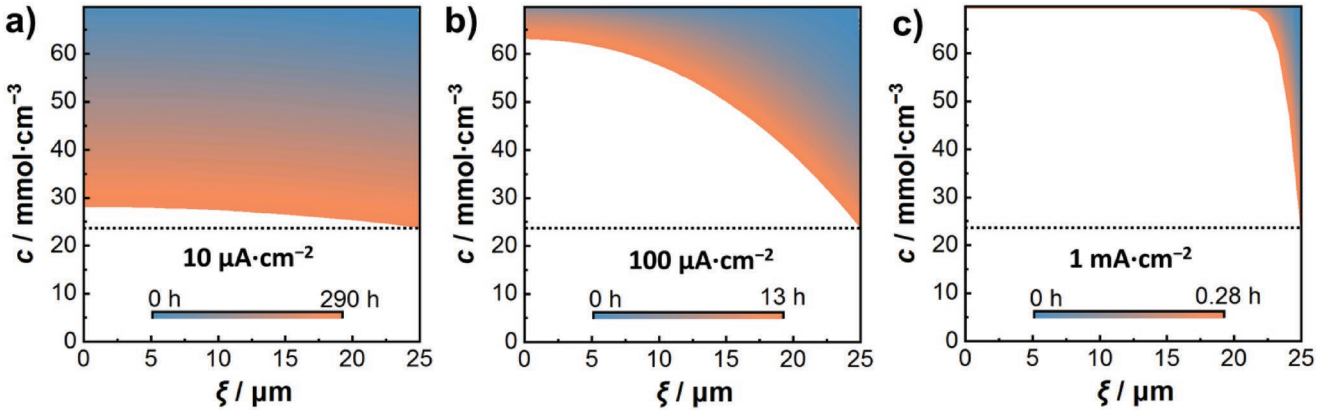

Figure 9. Simulation of the time-dependent concentration profile of a 25 µm thick $Li_{0.9}Mg_{0.1}$ anode at delithiation rates of a) i = 10 µA cm^{-2}, b) i = 100 µA cm^{-2}, and c) i = 1 mA cm^{-2}. The simulations were performed for time intervals at which the lithium concentration at $\xi = L$ = 25 µm does not fall below the miscibility window of the β-phase (see dotted line), which means that no unwanted phase segregation of the α-phase will have taken place at this point in time.

To examine the effect of temperature, the utilization was estimated as function of temperature for diffusion coefficients $\tilde{D}_{Li}(T)$ according to Equation (2)) in which E_A = 0.57 eV was used as estimated for lithium metal[64] (see Table S2, Supporting Information). The calculated diffusion coefficients are $\tilde{D}_{Li} = 3.9 \times 10^{-12}$, 1.7×10^{-10}, 9.5×10^{-10}, and 2.6×10^{-9} cm^2 s^{-1} at 0, 50, 80, and 100 °C, respectively. The chemical diffusion coefficient at 0 °C fits well with the effective diffusion coefficient $\tilde{D}_{Li} \approx 5.0 \times 10^{-12}$ cm^2 s^{-1} estimated experimentally at 0 °C using Sand's Equation. **Figure 10** shows the calculated lithium utilization of the β-phase as a function of temperature and current density. The utilization rises rapidly with increasing temperature. For current densities exceeding i = 1 mA cm^{-2}, temperatures higher than 80 °C are required to achieve a sufficiently high lithium utilization.

This shows that microstructural modifications or the embedding of the alloy into a porous host structure are required to enable lower operation temperatures.

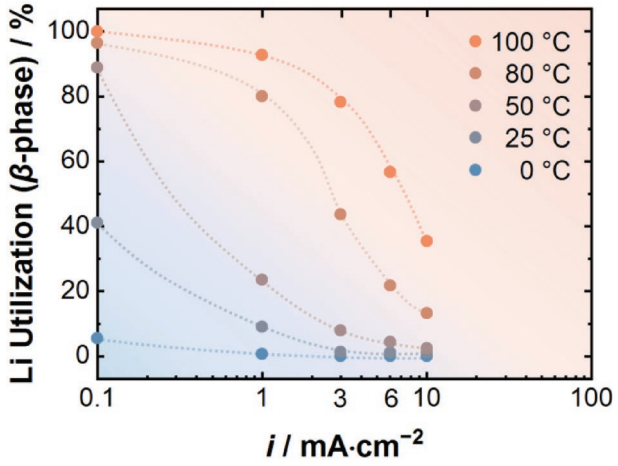

Figure 10. Temperature-dependent lithium utilization for delithiation of a $Li_{0.9}Mg_{0.1}$ alloy electrode calculated as a function of current density using the finite element method.

4. Conclusion

Macroscopic pore formation is the fundamental limitation of the lithium metal anode on solid electrolytes under anodic load. This limitation was found to be effectively prevented by alloying lithium with 10 at% Mg. However, the resulting Li–Mg alloy has its own kinetic limitation that is caused by the chemical diffusion of lithium in the alloy. The chemical diffusion coefficient is experimentally estimated to be about $\tilde{D}_{Li} = 3 \times 10^{-11}$ cm^2 s^{-1} for the β-phase in the Li–Mg system. The diffusion limitation restricts the rate capability of planar Li–Mg electrodes at room temperature to the double-digit µA cm^{-2} range. To meet advanced battery application requirements (i.e., 10 mA cm^{-2} for 5 mAh cm^{-2}), elevated temperatures higher than 80 °C were found to be required.

For a bare lithium metal anode, external pressure can effectively mitigate pore formation and thus the lithium depletion at the interface. However, high pressures in the MPa range are expected to achieve stable current densities ranging to 10 mA cm^{-2}, which will increase the cost and weight of battery stacks. However, an increased temperature will severely improve the diffusion kinetics as well as the plastic deformation rates of lithium. Thus, we conclude that already a slight increase in temperature may reduce the required stack pressure significantly.

For room temperature applications, new approaches need to be found to reduce the required stack pressures at high current densities for planar lithium metal anode designs. In this context, our work shows that the concentration of nonequilibrium defects in the Li (and Li alloy) anode has considerable impact on lithium stripping experiments[64] and needs to be understood in more depth for evaluating the rate capability of lithium metal anodes. We hope that our work serves to propel the assessment of lithium metal anodes in solid-state batteries.

5. Experimental Section

LLZO Specimen Preparation: Garnet powder of the composition $Li_{6.25}Al_{0.25}La_3Zr_2O_{12}$ was prepared by solid state synthesis of the starting materials Li_2CO_3 (>99.0%, Sigma-Aldrich), $La(OH)_3$ (99.9%,

Sigma-Aldrich), Al_2O_3 (99.8%, abcr), and ZrO_2 nanopowder (<100 nm, Sigma-Aldrich) at 1000 °C under oxygen atmosphere as reported previously.[26] Using a multistep heating schedule, isostatically pressed pellets were sintered for 5 h at 900 °C, 5 h at 1100 °C, and for 4 h at 1230 °C (100 °C h^{-1}) under dry oxygen to prevent carbonate formation and no trace carbonates are found on the surface of the pellets.[26] The pellets (diameter of 8.3 mm) had a relative density of 95% ± 1% and an ionic conductivity of (4.6 ± 0.4) × 10^{-4} S cm^{-1}. An in-depth characterization of the LLZO can be found in a previous work.[26]

Lithium and Li–Mg Alloy Synthesis and Characterization: Alloys of the composition $Li_{0.95}Mg_{0.05}$ and $Li_{0.9}Mg_{0.1}$ were prepared by a direct alloying method. Lithium metal rods (99.8%, abcr) were cut and pressed into thin lithium disks. Mg foil (0.15 mm thickness, 3 mm wide, ≥99.5%, Merck) was polished inside the glovebox, to remove the oxide layer, and sandwiched between the lithium disks. Around 100 mg of the mixture was then placed inside a homemade stainless steel crucible with an inner volume of 0.31 mL, closed with a stainless steel cover and heated for 4 h 100 °C above the liquidus temperature of the alloy (i.e., 420 and 450 °C for $Li_{0.95}Mg_{0.05}$ and $Li_{0.9}Mg_{0.1}$, respectively). Therefore, a heating plate (VWR International, VHP-C4) was used inside the glovebox. The alloy was then rapidly cooled down to room temperature. The bulk alloy was then successively pressed to foil with a thickness of 100 µm. Lithium metal working electrodes were similarly prepared by heating lithium metal inside the stain less steel crucible for 4 h at 380 °C. This was performed to ensure a similar thermal history of the lithium metal and the Li–Mg alloys to prevent large differences in the microstructure and defect concentration.

Lithium and the Li–Mg alloy anodes were structurally characterized by means of X-ray diffraction using an Empyrean powder diffractometer (PANalytical) with Cu K_α radiation (λ_1 = 1.5405980 Å, λ_2 = 1.5444260 Å, $I(\lambda_2)/I(\lambda_1)$ = 0.5). The anode foil samples were placed on a (911)-oriented silicon zero background holder and covered inside a glove box with Kapton polyimide film to avoid the reaction with humidity. Measurements were carried out in the 2θ range between 10° and 90° with a step size of 0.026°. The counting time per step was 200 s. To analyze the lattice parameter, a Pawley fit[65] was carried out using the TOPAS-Academic V6 software package (Bruker).[66] The profile was described using Thompson–Cox–Hasting pseudo-Voigt functions.

Cell Assembly and Electrochemical Measurements: To measure the dissolution kinetics of the lithium metal and the Li–Mg alloys, the method of an ideally reversible counter electrode was used to avoid the use of error-prone reference electrodes. In this setup, the counter electrode acts inherently also as reference electrode. The operation principle is described in detail in a previous publication.[26] In short, lithium metal foil was pressed at 400 MPa on both sides of a polished LLZO pellet to ensure a negligible small interface resistance. The oversized high pressure leads to full contact as reported in a previous work.[26] Then one lithium electrode was scraped off with a scalpel and the surface of the pellet was polished down to grit 1000 using SiC sandpaper. Then a Li–Mg alloy or lithium working electrode was pressed on the LLZO surface at much lower interface formation pressures. To enable a fair comparison between the dissolution kinetics of the different anode types, the initial contact with the LLZO pellet needs to be similar. Therefore, if not otherwise stated, the interface resistance was recorded in situ during pressing and the interface formation pressure was adjusted in a way that the resulting interface resistance was about 0.27 kΩ cm². The required formation pressure for the Li–Mg alloys was about 20 MPa—slightly higher than for pure lithium (≈15 MPa) due to higher material hardness.[59,67] The standard deviation of R_{int} was ± 0.05 kΩ cm^2 (see Table S1, Supporting Information). This strategy was used because relative changes of the interface for ideally contacted working electrodes ($R_{int} \approx$ 0 Ω·cm^2) would be invisible at the beginning of the measurement due to the resolution limit of impedance spectroscopy. The as assembled cells were sealed under argon into pouch cells and both electrodes were contacted using Ni-current collectors. For each measurement, a new working electrode was attached, while the counter electrode was retained. All measurements were performed in climate chambers under strict temperature control to prevent changes of the impedance due to temperature effects.

To gain comprehensive insights into the interface kinetics, current density, temperature, and pressure-dependent measurements were performed. GEIS was used to detect impedance changes operando during current load. Current densities of 50, 100, and 200 µA cm^{-2} were used. Measurements were performed using a VMP300 impedance analyzer (Bio-logic) in the frequency range between 7 MHz and 1 Hz with an AC amplitude that was set to 10% of the DC current density. To prevent too strong spectra distortion by violating the steady state condition, the spectrum acquisition was restricted to around 30 s. The cutoff potential was adjusted to 2, 4, and 6 V for 50, 100, and 200 µA cm^{-2}, respectively. Before each measurement, the OCV was recorded.

To investigate the effect of temperature, stripping measurements using GEIS were additionally conducted at 0 and 50 °C using a climate chamber (Weiss Klimatechnik).

Pressure-dependent stripping experiments were performed in a homemade setup. The setup was already reported in a previous work.[26] The pressure perpendicular to the interface was adjusted and recorded using an electronic force gauge (KMT55-20 kN). A metal spring prevents the relaxation of the pressure during the measurement. Pouch cells were placed into the inset of the cell setup. In order to avoid breaking the pellets during the measurement, rubber spacer discs with the radius of the pellet were placed on both sides. The applied force was thus normalized to the pellet area and not the lithium metal anode area.

CCDs were determined using GEIS. Lithium and Li–Mg alloy electrodes were therefore pressed at 400 MPa to achieve full contact and a negligible interface resistance on the working electrode side. The current density was increased by around 0.1 mA cm^{-2} per cycle. A stack pressure of 15 MPa was applied during the measurement.

Cycling experiments were performed on metal anodes that were intentionally only pressed with a low interface formation pressure to see the effect of anodic load on the short circuiting susceptibility. Galvanostatic electrochemical impedance spectroscopy with a DC current of 100 µA cm^{-2} was applied with a per-cycle areal capacity of 0.1 mAh cm^{-2}.

For relaxation experiments, the OCV of the cells was recorded immediately after the voltage during anodic load at 100 µA cm^{-2} reached a value of 4 V. Impedance spectra in the frequency range from 7 Mhz to 1 Hz were recorded intermediately every five minutes using a 10 mV perturbation voltage.

All impedance spectra were fit using the RelaxIS software package (rhd instruments, Version 3). To enable a stable fitting routine of the over 30.000 impedance spectra, some constraints were necessary. Therefore, the alpha value α for the constant phase element Q corresponding to the grain boundary charge transfer process was fixed to $\alpha \approx 0.9$, that was estimated with a previous PEIS measurement with higher resolution. Additionally, for some spectra, the low frequency part was neglected from impedance evaluation, if the steady state condition was violated (Kramers–Kronig test).

Ex Situ Scanning Electron Microscopy: For the investigation of the morphological changes of the lithium metal and Li–Mg alloy anode at the interfaces, the foil was detached after anodic load. Then the side facing the LLZO solid electrolyte was investigated using a Carl Zeiss Ultra field emission SEM instrument (Merlin). To prevent reaction with moisture, the samples were transferred from the glovebox to the vacuum chamber of the SEM with the Leica transfer module system (EM VCT500).

Diffusion Model Calculation with the Finite Element Method: The FEM was used to simulate the rate capability of a Li–Mg alloy anode of the starting composition of $Li_{0.9}Mg_{0.1}$. The "Transport of Diluted Species Module" of the COMSOL Multiphysics finite element software (version 5.2) was used for the calculations. The diffusion coefficient required for the modeling was estimated by comparison with the experimental data of the stripping experiment at 100 µA cm^{-2} and was found to be 3 × 10^{-11} cm^2 s^{-1} on average.

Supporting Information

Supporting Information is available from the Wiley Online Library or from the author.

Acknowledgements

This work was partly funded by the German Federal Ministry of Education and Research (BMBF) under the project "EvaBatt," grant identifier 03XP0134C and the project "LiSi," grant identifier 03XP0224E. T.K. acknowledges financial support (Kekulé scholarship) by the Funds of the Chemical Industry (FCI).

Conflict of Interest

The authors declare no conflict of interest.

Keywords

alloy electrode, lithium metal anode, solid-state battery, vacancy diffusion

Received: August 7, 2019
Revised: September 22, 2019
Published online: October 8, 2019

[1] J. Janek, W. G. Zeier, *Nat. Energy* **2016**, *1*, 16141.
[2] X.-B. Cheng, C.-Z. Zhao, Y.-X. Yao, H. Liu, Q. Zhang, *Chem* **2019**, *1*, 74.
[3] T. Placke, R. Kloepsch, S. Duehnen, M. Winter, *J. Solid State Electrochem.* **2017**, *21*, 1939.
[4] Y. Shen, Y. Zhang, S. Han, J. Wang, Z. Peng, L. Chen, *Joule* **2018**, *2*, 1674.
[5] X. Zhang, X. Chen, R. Xu, X. Cheng, H. Peng, R. Zhang, J. Huang, Q. Zhang, *Angew. Chem.* **2017**, *129*, 14395.
[6] D. Lin, Y. Liu, Y. Cui, *Nat. Nanotechnol.* **2017**, *12*, 194.
[7] J.-M. Tarascon, M. Armand, in *Materials For Sustainable Energy: A Collection of Peer-Reviewed Research and Review Articles from Nature Publishing Group*, World Scientific, Singapore **2011**, p. 171.
[8] G. Bieker, M. Winter, P. Bieker, *Phys. Chem. Chem. Phys.* **2015**, *17*, 8670.
[9] X. Wang, W. Zeng, L. Hong, W. Xu, H. Yang, F. Wang, H. Duan, M. Tang, H. Jiang, *Nat. Energy* **2018**, *3*, 227.
[10] M. Golozar, P. Hovington, A. Paolella, S. Bessette, M. Lagacé, P. Bouchard, H. Demers, R. Gauvin, K. Zaghib, *Nano Lett.* **2018**, *18*, 7583.
[11] S.-H. Yu, X. Huang, J. D. Brock, H. D. Abruña, *J. Am. Chem. Soc.* **2019**, *141*, 8441.
[12] C. Monroe, J. Newman, *J. Electrochem. Soc.* **2004**, *151*, A880.
[13] C. Monroe, J. Newman, *J. Electrochem. Soc.* **2005**, *152*, A396.
[14] S. Ramakumar, C. Deviannapoorani, L. Dhivya, L. S. Shankar, R. Murugan, *Prog. Mater. Sci.* **2017**, *88*, 325.
[15] Y. Zhu, J. G. Connell, S. Tepavcevic, P. Zapol, R. Garcia-Mendez, N. J. Taylor, J. Sakamoto, B. J. Ingram, L. A. Curtiss, J. W. Freeland, *Adv. Energy Mater.* **2019**, *9*, 1803440.
[16] H. Buschmann, J. Dölle, S. Berendts, A. Kuhn, P. Bottke, M. Wilkening, P. Heitjans, A. Senyshyn, H. Ehrenberg, A. Lotnyk, *Phys. Chem. Chem. Phys.* **2011**, *13*, 19378.
[17] K. Kerman, A. Luntz, V. Viswanathan, Y.-M. Chiang, Z. Chen, *J. Electrochem. Soc.* **2017**, *164*, A1731.
[18] A. Gurung, J. Pokharel, A. Baniya, R. Pathak, K. Chen, B. S. Lamsal, N. Ghimire, W.-H. Zhang, Y. Zhou, Q. Qiao, *Sustainable Energy Fuels* **2019**, https://doi.org/10.1039/C9SE00549H.
[19] E. J. Cheng, A. Sharafi, J. Sakamoto, *Electrochim. Acta* **2017**, *223*, 85.
[20] L. Porz, T. Swamy, B. W. Sheldon, D. Rettenwander, T. Frömling, H. L. Thaman, S. Berendts, R. Uecker, W. C. Carter, Y. Chiang, *Adv. Energy Mater.* **2017**, *7*, 1701003.
[21] Y. Ren, Y. Shen, Y. Lin, C.-W. Nan, *Electrochem. Commun.* **2015**, *57*, 27.
[22] F. Shen, M. Dixit, X. Xiao, K. Hatzell, *ACS Energy Lett.* **2018**, *3*, 1056.
[23] T. Swamy, R. Park, B. W. Sheldon, D. Rettenwander, L. Porz, S. Berendts, R. Uecker, W. C. Carter, Y.-M. Chiang, *J. Electrochem. Soc.* **2018**, *165*, A3648.
[24] T. Krauskopf, R. Dippel, H. Hartmann, K. Peppler, B. Mogwitz, F. H. Richter, W. G. Zeier, J. Janek, *Joule* **2019**, *3*, 2030.
[25] J. Kasemchainan, S. Zekoll, D. J. Spencer, Z. Ning, G. O. Hartley, J. Marrow, P. G. Bruce, *Nat. Mater.* **2019**, *18*, 1105.
[26] T. Krauskopf, H. Hartmann, W. G. Zeier, J. Janek, *ACS Appl. Mater. Interfaces* **2019**, *11*, 14463.
[27] A. Sharafi, E. Kazyak, A. L. Davis, S. Yu, T. Thompson, D. J. Siegel, N. P. Dasgupta, J. Sakamoto, *Chem. Mater.* **2017**, *29*, 7961.
[28] M. J. Wang, R. Choudhury, J. Sakamoto, *Joule* **2019**, *3*, 2165.
[29] S. Majoni, J. Janek, *Ber. Bunsen-Ges. Phys. Chem.* **1998**, *102*, 756.
[30] J. Janek, S. Majoni, *Ber. Bunsen-Ges. Phys. Chem.* **1995**, *99*, 14.
[31] P. Albertus, S. Babinec, S. Litzelman, A. Newman, *Nat. Energy* **2018**, *3*, 16.
[32] T. R. Jow, C. C. Liang, *J. Electrochem. Soc.* **1983**, *130*, 737.
[33] T. R. Jow, C. C. Liang, *Solid State Ionics* **1983**, *9–10*, 695.
[34] W. Luo, Y. Gong, Y. Zhu, Y. Li, Y. Yao, Y. Zhang, K. K. Fu, G. Pastel, C.-F. Lin, Y. Mo, E. D. Wachsman, L. Hu, *Adv. Mater.* **2017**, *29*, 1606042.
[35] K. K. Fu, Y. Gong, B. Liu, Y. Zhu, S. Xu, Y. Yao, W. Luo, C. Wang, S. D. Lacey, J. Dai, *Sci. Adv.* **2017**, *3*, e1601659.
[36] M. He, Z. Cui, C. Chen, Y. Li, X. Guo, *J. Mater. Chem. A* **2018**, *6*, 11463.
[37] C.-L. Tsai, V. Roddatis, C. V. Chandran, Q. Ma, S. Uhlenbruck, M. Bram, P. Heitjans, O. Guillon, *ACS Appl. Mater. Interfaces* **2016**, *8*, 10617.
[38] W. Luo, Y. Gong, Y. Zhu, K. K. Fu, J. Dai, S. D. Lacey, C. Wang, B. Liu, X. Han, Y. Mo, E. D. Wachsman, L. Hu, *J. Am. Chem. Soc.* **2016**, *138*, 12258.
[39] K. Fu, Y. Gong, Z. Fu, H. Xie, Y. Yao, B. Liu, M. Carter, E. Wachsman, L. Hu, *Angew. Chem., Int. Ed.* **2017**, *56*, 14942.
[40] W. Feng, X. Dong, P. Li, Y. Wang, Y. Xia, *J. Power Sources* **2019**, *419*, 91.
[41] M. Hiratani, K. Miyauchi, T. Kudo, *Solid State Ionics* **1988**, *28–30*, 1406.
[42] H. Koshikawa, S. Matsuda, K. Kamiya, M. Miyayama, Y. Kubo, K. Uosaki, K. Hashimoto, S. Nakanishi, *J. Electroanal. Chem.* **2019**, *835*, 143.
[43] J. Dai, C. Yang, C. Wang, G. Pastel, L. Hu, *Adv. Mater.* **2018**.
[44] C. Yang, H. Xie, W. Ping, K. Fu, B. Liu, J. Rao, J. Dai, C. Wang, G. Pastel, L. Hu, *Adv. Mater.* **2018**, *31*, 1804815.
[45] M. N. Obrovac, V. L. Chevrier, *Chem. Rev.* **2014**, *114*, 11444.
[46] C.-M. Park, Y.-U. Kim, H. Kim, H.-J. Sohn, *J. Power Sources* **2006**, *158*, 1451.
[47] M. Jagannathan, K. R. Chandran, *J. Electrochem. Soc.* **2013**, *160*, A1922.
[48] L. Kong, L. Wang, Z. Ni, S. Liu, G. Li, X. Gao, *Adv. Funct. Mater.* **2019**, *29*, 1808756.
[49] F. H. Herbstein, B. L. Averbach, *Acta Metall.* **1956**, *4*, 407.
[50] D. W. Levinson, *Acta Metall.* **1955**, *3*, 294.
[51] A. A. Nayeb-Hashemi, J. B. Clark, A. D. Pelton, *Bull. Alloy Phase Diagrams* **1984**, *5*, 365.
[52] Y. Iwadate, M. Lassouani, F. Lantelme, M. Chemla, *J. Appl. Electrochem.* **1987**, *17*, 385.
[53] D. G. Kevorkov, J. Gröbner, R. Schmid-Fetzer, V. V. Pavlyuk, G. S. Dmytriv, O. I. Bodak, *J. Phase Equilib.* **2001**, *22*, 34.
[54] H. J. Sand, *Philos. Mag.* **1901**, *1*, 45.
[55] P. Haasen, *Physical Metallurgy*, 3rd ed., Cambridge University Press, Cambridge, USA **1996**.
[56] P. Shewmon, *Diffusion in Solids*, Springer, Cham, Swizerland **2016**.

[57] *Self-Diffusion, Solute-Diffusion and Interdiffusion in Binary Intermetallics* (Ed: H. Mehrer), Trans Tech Publ, Zurich, Swizerland **2014**.
[58] M. Rohnke, C. Rosenkranz, J. Janek, *Solid State Ionics* **2006**, *177*, 447.
[59] J. Trivisonno, C. S. Smith, *Acta Metall.* **1961**, *9*, 1064.
[60] W. S. LePage, Y. Chen, E. Kazyak, K.-H. Chen, A. J. Sanchez, A. Poli, E. M. Arruda, M. D. Thouless, N. P. Dasgupta, *J. Electrochem. Soc.* **2019**, *166*, A89.
[61] A. Masias, N. Felten, R. Garcia-Mendez, J. Wolfenstine, J. Sakamoto, *J. Mater. Sci.* **2018**, *166*, A89.
[62] A. Sharafi, C. G. Haslam, R. D. Kerns, J. Wolfenstine, J. Sakamoto, *J. Mater. Chem. A* **2017**, *5*, 21491.
[63] Y. Zhang, K. R. Chandran, M. Jagannathan, H. Z. Bilheux, J. C. Bilheux, *J. Electrochem. Soc.* **2017**, *164*, A28.
[64] D. M. Fischer, P. Duwe, S. Indris, P. Heitjans, *Solid State Nucl. Magn. Reson.* **2004**, *26*, 74.
[65] G. S. Pawley, *J. Appl. Crystallogr.* **1981**, *14*, 357.
[66] A. A. Coelho, *Coelho Software*, Brisbane, Australia **2007**.
[67] Y.-M. Kim, I.-H. Jung, B.-J. Lee, *Modell. Simul. Mater. Sci. Eng.* **2012**, *20*, 035005.